Metaheuristic Rock Property Determination Driven by Rock Type Constrained Global N-Dimensional Analysis*

Travis Ramsay[1], Chang Lu[1], and Jie He[1]

Search and Discovery Article #42292 (2018)**
Posted October 29, 2018

*Adapted from extended abstract based on oral presentation given at 2018 AAPG Annual Convention & Exhibition, Salt Lake City, Utah, May 20-23, 2018
 DOI:10.1306/42292Ramsay2018

[1]Halliburton, Houston, Texas (Travis.Ramsay@halliburton.com)

Abstract

The simulation-to-seismic process leverages a petro-elastic model (PEM) to maintain the continuity of the simulator response with the seismic inversion. The requisite dry rock properties in the PEM are typically derived from measurements made on core samples or reference descriptions. Dry rock property descriptions from extracted core are often missing or limited because of cost and/or operational time constraints that cause a small data challenge. A small data challenge is recognized when there is an overabundance of some data, but a complete lack of the desired data to accomplish the objective of reconciling the flow simulator response with the seismic data. A rock-type driven global dimensional optimization technique is used directly on 3D geocellular arrays to determine dynamic elastic properties from the reservoir simulator.

Integrated rock typing and global N-dimensional optimization is used in a field case involving ill-posed petro-elastic characterization to develop a PEM for the simulator. This work shows how global N-dimensional optimization can be improved by the inclusion of electrofacies defined as rock types, and then used to fine tune the PEM for seismic driven history matching.

Rock typing is used here to accelerate a metaheuristic optimization process where the design variables and optimal solution are derived from 3D arrays that minimize the necessity for stochastic computation. While this process is examined specifically for the PEM, it also can be applied to other data limited modeling challenges.

Introduction

PEM is used extensively in integrated closed-loop 4D seismic for simulation solutions to reconcile simulated production induced phenomena to time-lapse seismic (Ramsay et al., 2016; Emerick et al., 2007; MacBeth et al., 2016). Classic usage of the PEM has been as part of post-processing the saturation, density, and pressure results from the reservoir simulator at user defined time intervals. However, recent efforts have focused on embedding the PEM directly into the reservoir simulator so that dynamic elastic properties can be computed simultaneously with

typical results of the reservoir simulator (Landmark, 2017). Although these efforts greatly simplify the functional aspects of the workflow, there are caveats that characterize it as a small data challenge.

Small data challenges are a contemporaneous countermeasure to big data. Here, emphasis is placed on analyzing an overabundance of some data types to derive or infer those that are limited or significantly lacking (You et al., 2017). The necessary properties for building a PEM are dry rock density, bulk modulus, and shear modulus; however, these properties are typically obtained from mechanical tests conducted in a physical laboratory on a core sample.

Performing such tests is time consuming and involves cost; so, frequently, they are not performed. As a result, the desire to conduct integrated closed-loop workflow can be significantly obstructed. The proposed solution helps enable the execution of these closed-loop integrated workflows by computing missing properties based upon governing physical relations and deriving an optimal solution for using the computed properties to mimic observed data.

The solution uses an instance of N-dimensional optimization based on a metaheuristic optimization process. This study focuses on a modified particle swarm optimization (PSO) with an applied external penalty function (EPF). The modifications to the PSO and EPF are the N-dimensional characterization of design variables and the classification of rock types in the model to constrain the search for an optimal solution.

In this implementation, PSO uses the position of moving particles in a bounded solution space to identify the optimal solution to a pseudo-objective function. The particles move in the N-dimensional design space by positional updates computed as functions of particle velocity. Multiple realizations of the PSO and EPF are executed so that the derivation of an optimal solution for the desired properties can be further analyzed on a gridblock-by-gridblock basis in the 3D geocellular array.

Theory

A metaheuristic PSO method with EPF is developed to solve an ill-posed elastic property challenge leading to the characterization of rock properties for the execution of dynamic elastic properties via an embedded PEM in a reservoir simulator. In particular, variable neighborhood search (VNS) and PSO are combined in a variable neighbor particle swarm optimization (VNPSO) to solve the multi-objective problem following Haupt and Haupt (2004) and Abraham et al. (2006). The advantage of VNS is that it depends on iteratively exploring regions, or neighborhoods, of increasing size in the design variable space to improve the determination of an optimum solution with shaking strategies (Hansen and Mladenovic, 2001; Hansen and Mladenovic, 2003). The classic PSO method is comprised of a random initialization swarm of particles within a population of potential solutions. During each iteration, the particles move iteratively through the N-dimensional problem space to search for new solutions as illustrated in a single iteration of a nominal optimization problem in Figure 1. The VNPSO method is further characterized by the use of the “gbest model,” following Kennedy and Eberhart (2001). In the gbest model, each particle trajectory is influenced by the best point found by any particle in the population.

The VNPSO is guided by EPF through multidimensional pseudo-objective functions to simultaneously compute dry rock property models in a small data challenge. Here, the challenge is prescribed as small data because there is a lack of dry rock density and elastic property descriptions

of the formation. The objective is to use optimization to simultaneously identify the dry rock properties that are needed for the execution of a PEM in a reservoir simulation model. While VNPSO and EPF are executed in this work, other statistical optimization and filtering techniques can also be applied to enable a solution to this challenge, including genetic algorithms, Markov chain Monte Carlo, Kalman, and Sequential Monte Carlo.

In general, the pseudo-objective function is described in Eq. 1:

$$\Phi\left(\bar{x}, r_p\right) = F(\bar{x}) + r_p P(\bar{x}) \quad (1)$$

The term $F(\bar{x})$ represents the original objective function, which is constituted as the L2 Norm of p-impedance, considering seismic inversion (Z_p^{inv}) as the true representation and an optimal p-impedance computed by the VNPSO (Z_p^{opt}). The objective function is described in Eq. 2 as:

$$F(\bar{x}) = \left|Z_p^{inv} - Z_p^{opt}\right| \quad (2)$$

The description of the objective function in this manner suggests two important points about the application of VNPSO. First, p-impedance computed by seismic inversion is a critical component to constrain the determination of an optimal solution. Secondly, there is a requirement of physics derived, an empirical or constitutive relationship to which p-impedance can be computed from disparate data sources. The use of seismic inversion derived p-impedance is critical but not required, because the VNPSO can also be executed in an unconstrained manner using a completely stochastic implementation. However, it should be noted that the omission of the seismic derived impedance from the objective function could significantly increase the uncertainty of the final result. Given this consideration, this work focuses on the seismic inversion constraint. The physics driven relations necessary to relate dry and saturated rock properties are typically associated with the Gassmann equation (Emerick et al., 2007; Mavko et al., 2009), which is shown in Eq. 3:

$$\frac{1}{K_{sat}} = \frac{1}{K_{mineral}} + \frac{\varphi}{K_\varphi + \frac{K_{mineral} K_{fluid}}{K_{mineral} - K_{fluid}}} \quad (3)$$

The Gassmann relation involves the superposition of the inverse of the mineral bulk modulus and the inverse of the pore space stiffness modified by fluids, which results in the bulk modulus of the saturated pore space K_{sat}. The fluid bulk modulus K_{fluid} is computed based on Wood's equation and describes the saturation-weighted inverse bulk modulus of the formation fluid using harmonic averaging, expressed in Eq. 4 as:

$$\frac{1}{K_{fluid}} = \frac{S_{water}}{K_{water}} + \frac{S_{oil}}{K_{oil}} + \frac{S_{gas}}{K_{gas}};\ for\ S_{water} + S_{oil} + S_{gas} = 1 \quad (4)$$

The term $\frac{1}{K_{fluid}}$ describes the total fluid compressibility, which is similarly used in reservoir simulators in the determination of saturated pore space properties (Landmark, 2017). The dry rock modulus K_{dry} describes porous media drained of fluid and is computed according to Eq. 5 as:

$$\frac{1}{K_{dry}} = \frac{1}{K_{mineral}} + \frac{\varphi}{K_{\varphi}} \; where \; \frac{1}{K_{\varphi}} = \frac{1}{v_{pore}} \frac{\partial v_{pore}}{\partial \sigma} \quad (5)$$

The bulk modulus of the intrinsic mineral of the porous media is described as $K_{mineral}$, the stress induced by pore pressure is σ, and the time dependent effective porosity (adjusted by the net-to-gross and pore volume multiplier computed from rock compaction) is φ. Analogous to the fluid bulk modulus is the inverse pore space bulk modulus $\frac{1}{K_{\varphi}}$, which can also be expressed as compressibility C_{φ} following Eq. 6:

$$C_{\varphi} = \frac{1}{K_{\varphi}} = \frac{1}{v_{pore}} \frac{\partial v_{pore}}{\partial \sigma} \quad (6)$$

A penalty correction term r_p is a multiplier applied to the EPF term $P(\bar{x})$, so it increases in magnitude for each solution of $\bar{x}^*$ as the "best" solution is found with each iteration of the updated pseudo-objective function (Arora, 2012). The penalty function is described in Eq. 7 according to:

$$P(\bar{x}) = \sum_{j=1}^{m} \{\max(0, g_j(\bar{x})\}^2 + \sum_{k=1}^{l} \left(h_k(\bar{x})\right)^2 \quad (7)$$

The $g_i(\bar{X})$ functions are characterized as inequality constraints, while the $h_j(\bar{X})$ functions are characterized as equality constraints. Because of the use of EPF, it is important to note the N-dimensional constraint boundaries can constitute solutions to the optimization of the pseudo-objective function.

The problem statement defining the optimization problem is described in Eq. 8 for the simultaneous determination of dry rock bulk modulus, shear modulus, and matrix density as 3D geocellular arrays:

$$Minimize \; \Phi\left(\bar{x}, r_p\right) \quad (8)$$

where Z_p^{opt} of Eq. 2 is computed as

$$Z_p^{opt} = \rho_{sat} \sqrt{\frac{K_{sat} + \frac{4}{3} G_{sat}}{\rho_{sat}}} \quad (9)$$

so that

$$g_1(\bar{X}):\ K_{sat} - \left(\frac{1}{K_{mineral}} + \frac{\varphi}{K_\varphi + \frac{K_{mineral} K_{fluid}}{K_{mineral} - K_{fluid}}} \right)^{-1} \leq 0 \quad (10)$$

$$g_2(\bar{X}):\ K_{sat} - \rho_{sat} \left(V_p^2 - \frac{4}{3\rho_{sat}} G_{dry} \right) \leq 0 \quad (11)$$

$$g_3(\bar{X}):\ \ G_{dry} - \rho_{sat} V_s^2 \leq 0 \quad (12)$$

$$h_1(\bar{X}):\ \rho_{matrix} - \left(\sum_{i=1}^{4} V_i \rho_i \right) = 0 \quad (13)$$

$$h_2(\bar{X}):\ K_{matrix} - \left[2 \left\{ \sum_{i=1}^{4} V_i K_i + \left(\sum_{i=1}^{4} \frac{V_i}{K_i} \right)^{-1} \right\}^{-1} + \frac{\varphi}{K_\varphi} \right]^{-1} = 0 \quad (14)$$

The $g_1(\bar{X})$ inequality constraint describes the saturated rock bulk modulus. The $g_2(\bar{X})$ inequality constraint expresses the compressional velocity constraint in the saturated porous media. The compressional wave velocity is V_p, the saturated density is ρ_{sat}, and the dry rock shear modulus is G_{dry}. Under Gassmann assumptions, G_{dry} is equal to the saturated shear modulus G_{sat}. The $g_3(\bar{X})$ inequality constraint describes the dry mineral shear modulus; here, the shear wave velocity is V_s. The $h_1(\bar{X})$ equality constraint characterizes the matrix density equation; the mineral volume fraction is V_i, and the component matrix density is ρ_i. The $h_2(\bar{X})$ equality constraint represents the Voigt-Reuss-Hill average for the mineral bulk modulus; the rock type component bulk modulus is K_i. The consideration of rock types is implemented here as the ith member in the devised rock type set. It is this rock type set that yields the additional $h_1(\bar{X})$ and $h_2(\bar{X})$ equality constraints, which are based on rock typing characterization and include assessed volume fraction (V_i), dry rock matrix density (ρ_i), and bulk modulus of the rock (K_i). The bulk modulus of the dry rock K_{matrix} is equivalent to K_{dry}. The optimal solution for 3D geocellular arrays for K_{matrix}, G_{dry}, and ρ_{matrix} is then determined by the combined VNPSO and EPF scheme.

EPF is part of a group of sequential unconstrained minimization techniques (SUMT) that constitute equality and inequality constraint equations that are combined with an objective function to derive a pseudo-objective function. SUMT are comprised of EPF and interior penalty function (IPF) methods. EPF was used in this work because it is more simplistic and does not require the boundary condition maintenance like IPF, which has asymptotic behavior manifest on the solution boundary of its constraint equations.

The rock types were characterized following an electrofacies description analogous to the petrofacies in Ramsay and Yarus (2015) and are shown in Figure 2. It is evident that four electrofacies exist; these are defined (by color index) as siltstone (high porosity), siltstone (low porosity), shale, and dolomite.

The significance of consistent petrofacies and electrofacies descriptions in rock type definitions for reservoir simulation have been clearly established (Ramsay and Yarus, 2015). Here, the rock types are used in the acceleration of the optimization process by increasing the constraint equations by two; the two specific constraint equations that were added are the equality constraints (Eqs. 13 and 14). This reduces the a priori need for particles in the VNPSO to search a larger solution space with fewer bounds and increases the physical realism of the optimal solution. Thus, the inclusion of rock types reduces stochastic computation requirements for a given model execution and helps ensure the estimated elastic and density properties are consistent with electrofacies defined rock types. This has significant value for the continued execution of a seismic history matching workflow where consistency between geophysics, earth modeling, and reservoir simulation data is desired.

Results

Twenty realizations of the combined VNPSO and EPF were executed with the enforced rock type constraints. Because of the simultaneous process associated with the computation of the three respective PEM arrays (K_{matrix}, G_{dry}, and ρ_{matrix}) for single realization, a total of 60 arrays were generated analogous to the process highlighted in Figure 3. The 3D geocellular array described by Z_p^{inv} (p-impedance by seismic inversion) in the optimization process is shown in Figure 4. Rescaling was performed for the sake of presentation and is also evident by the excessively low and high values of p-impedance in the array. The rock type constrained VNPSO and EPF involved computing the L2 Norm with this p-impedance, derived by seismic inversion, representing the measured result. The exemplary PEM arrays from realization 13 are shown in Figure 5. It is clear from observing the optimized PEM arrays and the p-impedance by seismic inversion that the long wavelength variation in the spatial distribution of properties is consistent. Additionally, the spatial distribution of properties between respective PEM properties are in near complete agreement, except for isolated shorter wavelength variations. It is important to note the similarity in spatial distribution of properties is attributed to the rock type classification, which not only enabled grouping according to electrofacies but also expedited the VNPSO and EPF process.

The execution of multiple realizations enabled analysis of the variation in the optimal solution obtained across individual gridblocks in the computed arrays. The geocellular grid has dimensions of 34×47×125 gridblocks. Results were further analyzed for four specific gridblocks in the 3D geocellular grid listed according to location (I, J, K): gridblock (17, 1, 1), gridblock (12, 35, 85), gridblock (32, 21, 32), and gridblock (17, 5, 109). These gridblocks were specifically selected because they represented characterizations of each rock type. It is important to note that each realization is independent and uncorrelated with other realizations but the optimized rock properties are correlated for a given realization.

The results for the dry rock bulk modulus are shown in Figure 6. In Figure 6a the optimal solutions for 19 of the 20 realizations in gridblock (17, 1, 1) were above 2e6 psi, suggesting that realization 2 yielded an outlier solution that represents the identification of a local minima in the L2 Norm solution space. The solutions in gridblock (12, 35, 85) are well distributed in the 2e6 to 8e6 psi range according to Figure 6b, which suggests the results below 2e6 psi are potentially extraneous. There were greater quantities of optimal solutions for gridblock (32, 21, 32) found in the numerical range above 4.5e6 psi, with only a few solutions obtained below 4.5e6 psi according to Figure 6c. Gridblock (17, 5, 109) demonstrated a sufficient spread of optimal solutions in Figure 6d; however, the bulk of the results were below 6e6 psi.

The numerical range of the computed shear bulk modulus was narrower when compared to the dry rock bulk modulus. The distribution of G_{dry} is shown in Figure 7 for the four noted observation gridblocks. It is observed that gridblock (17, 1, 1) has five outlier G_{dry} estimates at realizations 1, 2, 6, 13, and 16 in Figure 7a. This is clear by observing that a majority of the optimal solutions are located in the numerical range of 1.2e6 to 3e6 psi in the solution space. All other computed shear bulk moduli for the remaining gridblocks are similarly spread throughout the solution space with three to five outliers existing out of the 20 realizations. The numerical range for the dry rock matrix density is rather well contained as illustrated in Figure 8. Dry rock matrix density is computed to be between 135 and 180 lbm/ft^3 for all 20 realizations.

The narrower spread of optimal petro-elastic model parameters in Figure 6c, Figure 7c, and Figure 8c suggests increased assurance in rock type characteristic matching for gridblock (32, 21, 32) compared exclusively to the other gridblocks that were analyzed. Greater spread in the optimal determination of properties for other gridblocks implies larger degrees of uncertainty in the a priori determination of rock type by electrofacies. The summary statistics associated with Figure 6, Figure 7, and Figure 8 are shown in Table 1 for reference. Comparison of the results considering the rock types ascribed to each observation gridblock suggests consistent characterization of K_{matrix}, G_{dry}, and ρ_{matrix} for most cases. The exception is the computed shear modulus of shale [gridblock (32, 21, 32)] where the solution differs significantly from that of referenced mechanical tests according to Manger (1963) and Lama and Vutukuri (1978). However, it should be noted this is the examination of one gridblock for a given rock type and further analysis of all optimized values for a given rock type would be addressed in future work.

Conclusions

An N-dimensional metaheuristic optimization solution was used with a rock type constraint on 3D geocellular data to facilitate the optimal determination of petro-elastic rock property parameters with the requisite purpose of executing a simulation-to-seismic process. The application of the method represents a solution to a small data challenge, as described by You et al. (2017), where the availability of data of interest is severely limited or lacking but explicit physical relationships are leveraged to infer properties of interest by optimization. The VNPSO and EPF were used for an ill-posed PEM parameter characterization for the purpose of executing a closed-loop simulation-to-seismic solution. The optimization process results demonstrated appreciable short and long wavelength similarities, which leads to preferred matching of the optimized properties when used to compute the L2 Norm of p-impedance. Rock types were found to improve the consistency in the distribution of K_{matrix}, G_{dry}, and ρ_{matrix}. Future work is needed to assess all optimized solutions for the requisite rock elastic properties in addition to the exemplary analysis conducted for one gridblock per rock type. Additionally, the rock type constraints bounded the search for an optimal solution, which decreased the size of the design space for the particles in the PSO to traverse given the enforced solution tolerances. While some local disparities existed in the estimated dry rock properties, they are judged relative to the value of executing the intended 4D workflow and the time to iteratively evaluate the pseudo-objective function. As a result, they are deemed acceptable considering the tradeoff between the value of information, workflow efficiency, and solution accuracy.

References Cited

Abraham, A., H. Liu, and T.-G. Chang, 2006, Variable neighborhood particle swarm optimization algorithm: Genetic and Evolutionary Computations Conference (GECCO), Seattle, Washington, July 8-12.

Arora, J., 2012, Introduction to Optimum Design: Academic Press.

Emerick, A., R. Jesus de Moraes, and J. Rodrigues, 2007, Calculating seismic attributes within a reservoir flow simulator: Latin American & Caribbean Petroleum Engineering Conference, Buenos Aires, Argentina, April 5-18, SPE-107001-MS.

Hansen, P., and N. Mladenovic, 2001, Variable neighbourhood search: Principles and applications: European Journal of Operations Research, v. 130, p. 449-467.

Hansen, P., and N. Mladenovic, 2003, Variable neighbourhood search, *in* F.W. Glover, and G.A. Kochenberger, eds., Handbook of Metaheuristics, Dordrecht, Kluwer Academic Publishers.

Haupt, R., and S. Haupt, 2004, Practical Genetic Algorithms, Wiley-Interscience.

Kennedy, J., and R. Eberhart, 2001, Swarm Intelligence, Morgan Kaufmann.

Lama, R.D., and V.S. Vutukuri, 1978, Handbook on Mechanical Properties of Rocks, 2nd Edition, Trans Tech Publications, Switzerland.

Landmark Software and Solutions, 2017, Nexus User Manual, Houston, Texas.

MacBeth, C., C. Geng, and R. Chassagne, 2016, A fast-track simulator to seismic proxy for quantitative 4D seismic analysis: SEG International Exposition and 86th Annual Meeting, Dallas, Texas, October 16-21.

Manger, G.E., 1963, Porosity and bulk density of sedimentary rocks: U.S. Geological Survey Bulletin 1144-E.

Mavko, G., T. Mukerji, and J. Dvorkin, 2009, The Rock Physics Handbook, Tools for Seismic Analysis of Porous Media, Cambridge University Press.

Ramsay, T., and J. Yarus, 2015, Petrofacies determination in unconventional reservoirs driven by a simulation-to-seismic process: EUROPEC, Madrid, Spain, June 1-4, SPE-174295-MS.

Ramsay, T., J. Lomask, and J. Ting, 2016, Seismic through simulation with integrated time-lapse workflow: AAPG/SEG International Conference & Exhibition, Cancun, Mexico, September 6-9.

You, Y., J. Li, and N. Xu, 2017, A constrained parameter evolutionary learning algorithm for Bayesian Network under incomplete and small data: 36th Chinese Control Conference (CCC), Dalian, China, July 26-28, p. 3044-3051.

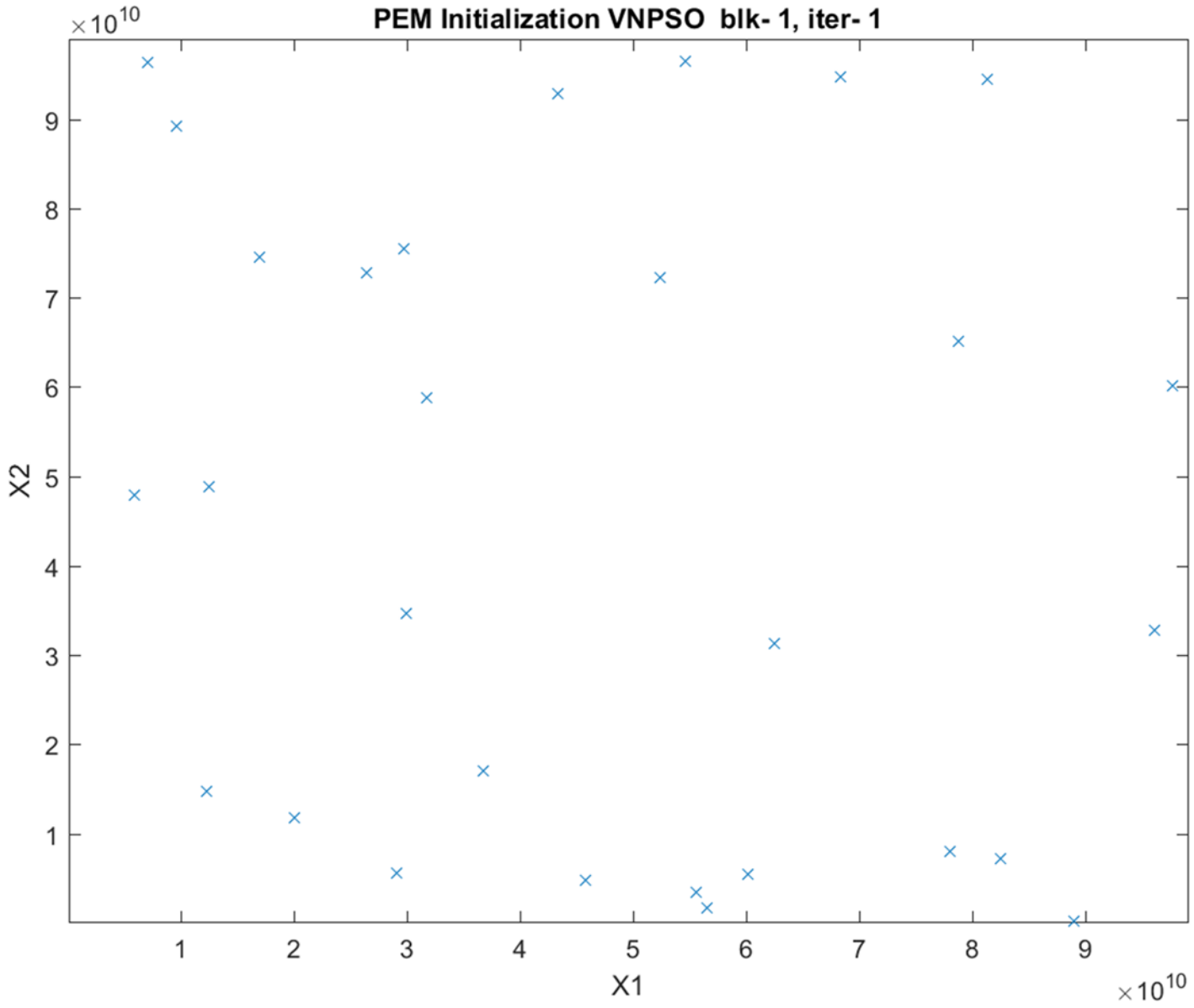

Figure 1. Illustration of swarm particles distributed in the solution space of X1 and X2 design variables.

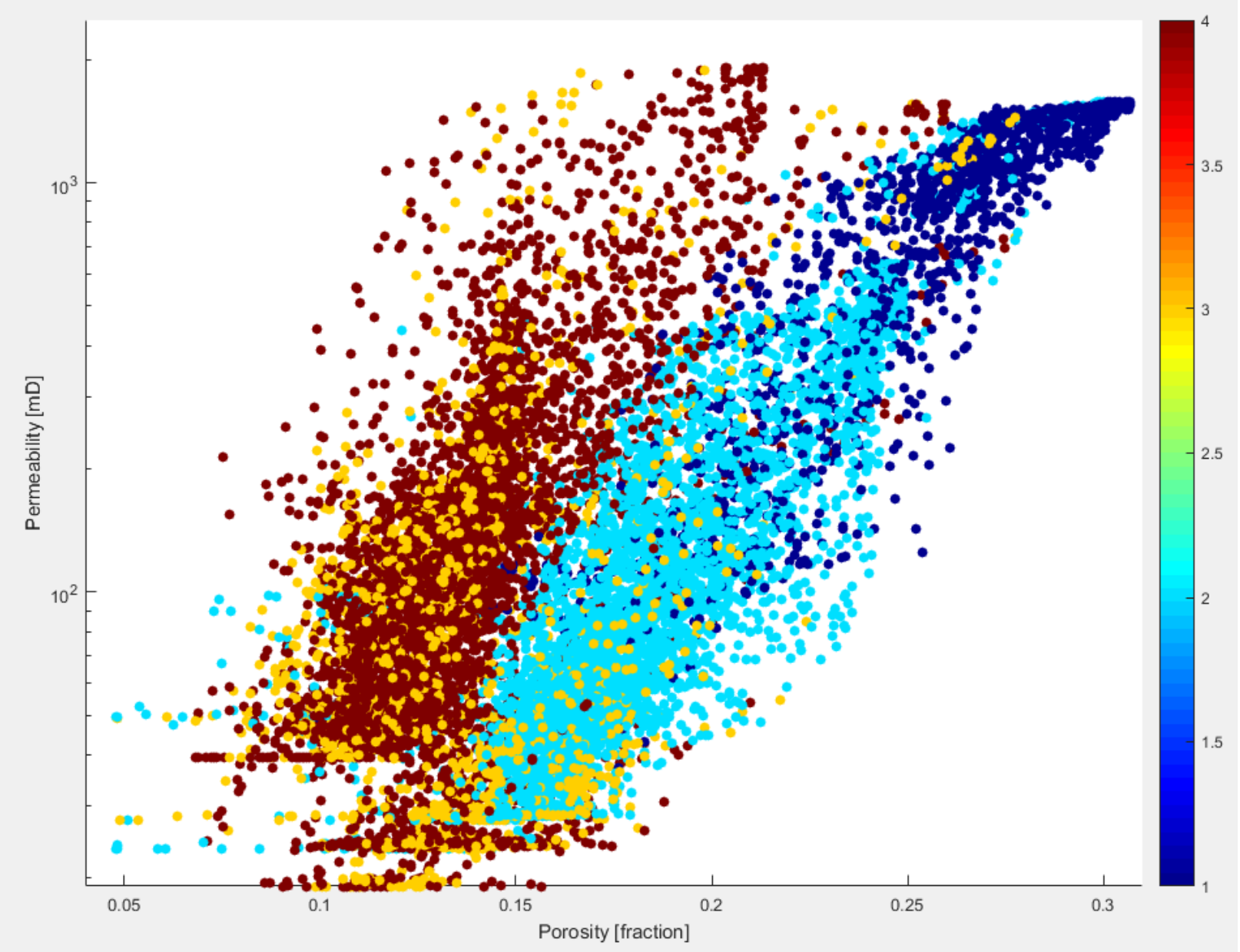

Figure 2. Crossplot of Porosity vs. Permeability colored by electrofacies; colored rock types are high porosity siltstone (dark blue), low porosity siltstone (light blue), shale (light orange), and dolomite (dark red).

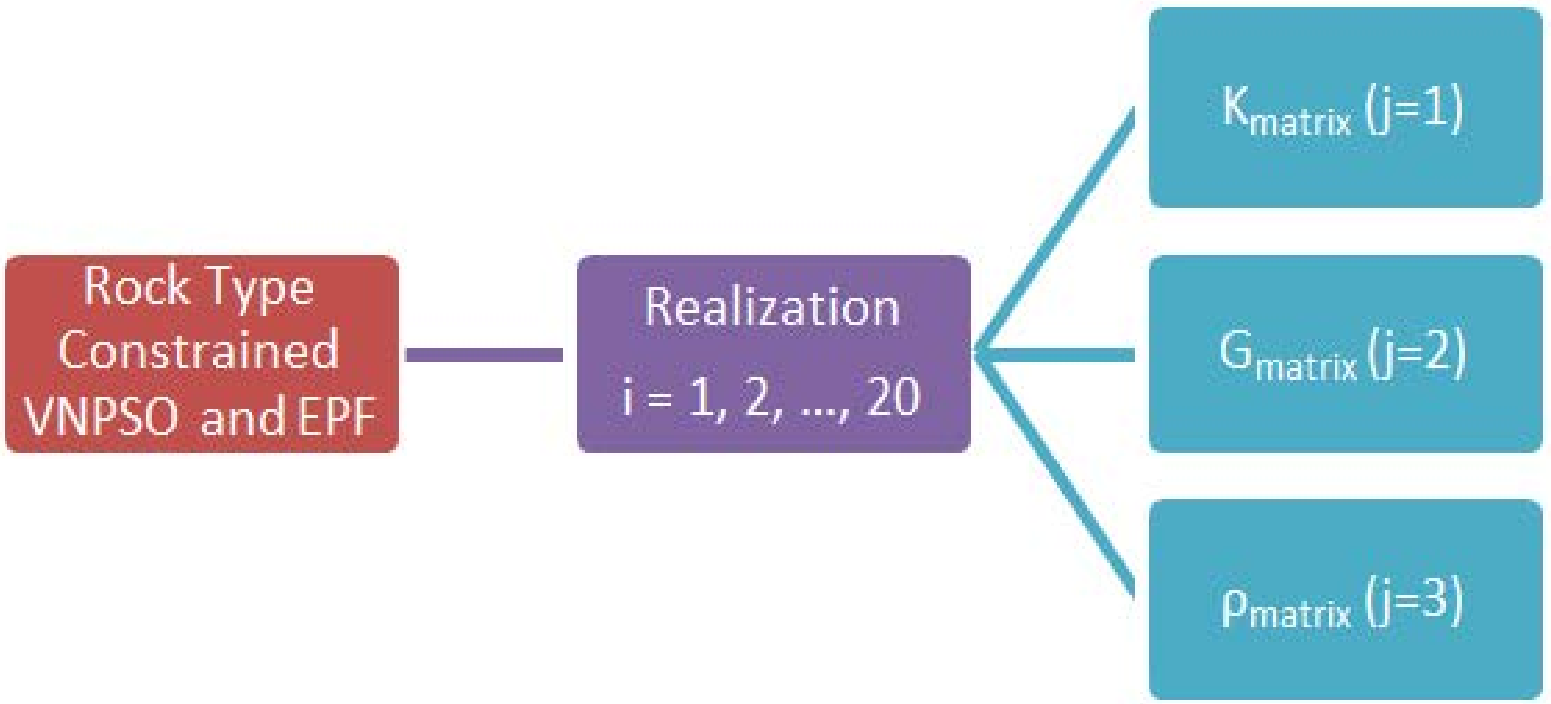

Figure 3. Realization Matrix for rock type constrained VNPSO and EPF showing Realization Index and Optimized PEM Arrays.

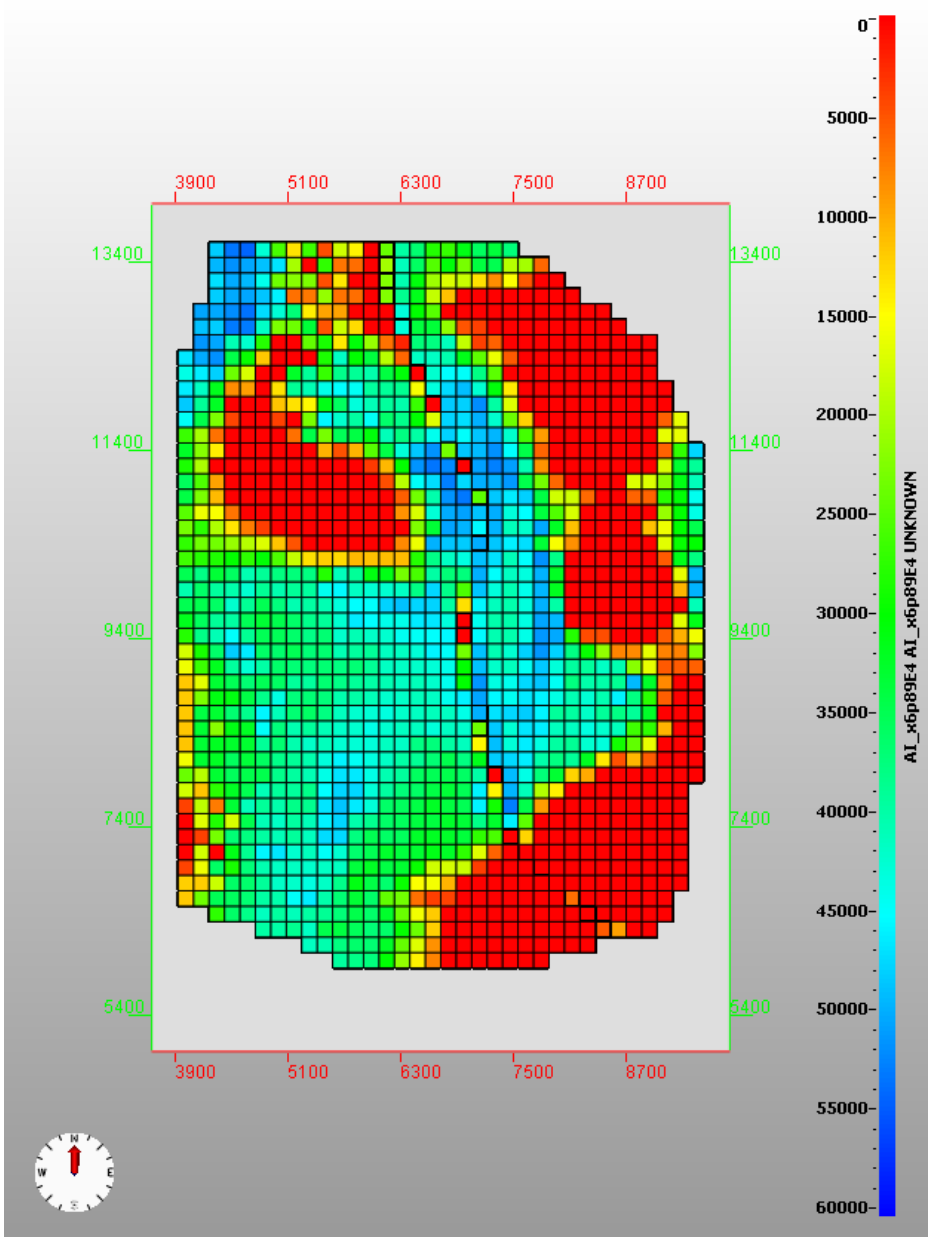

Figure 4. Synthetically scaled 3D geocellular P-Impedance Array used in the execution of the combined VNPSO and EPF model. Scaling is performed to protect the privacy of the data source.

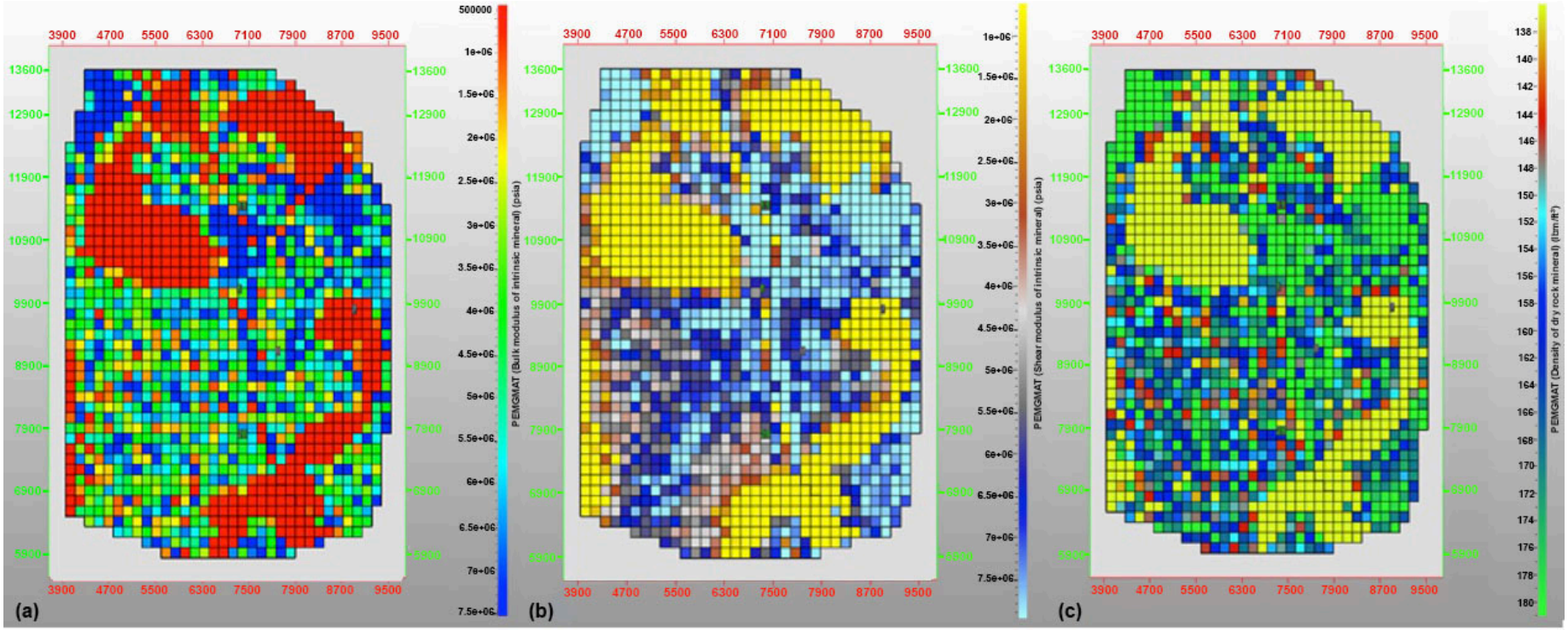

Figure 5. Realization for Run 13 illustrating the generated 3D Geocellular Arrays for the optimized solution of (a) Kmatrix, (b) G_dry, and (c) ρ_matrix using the combined VNPSO and EPF.

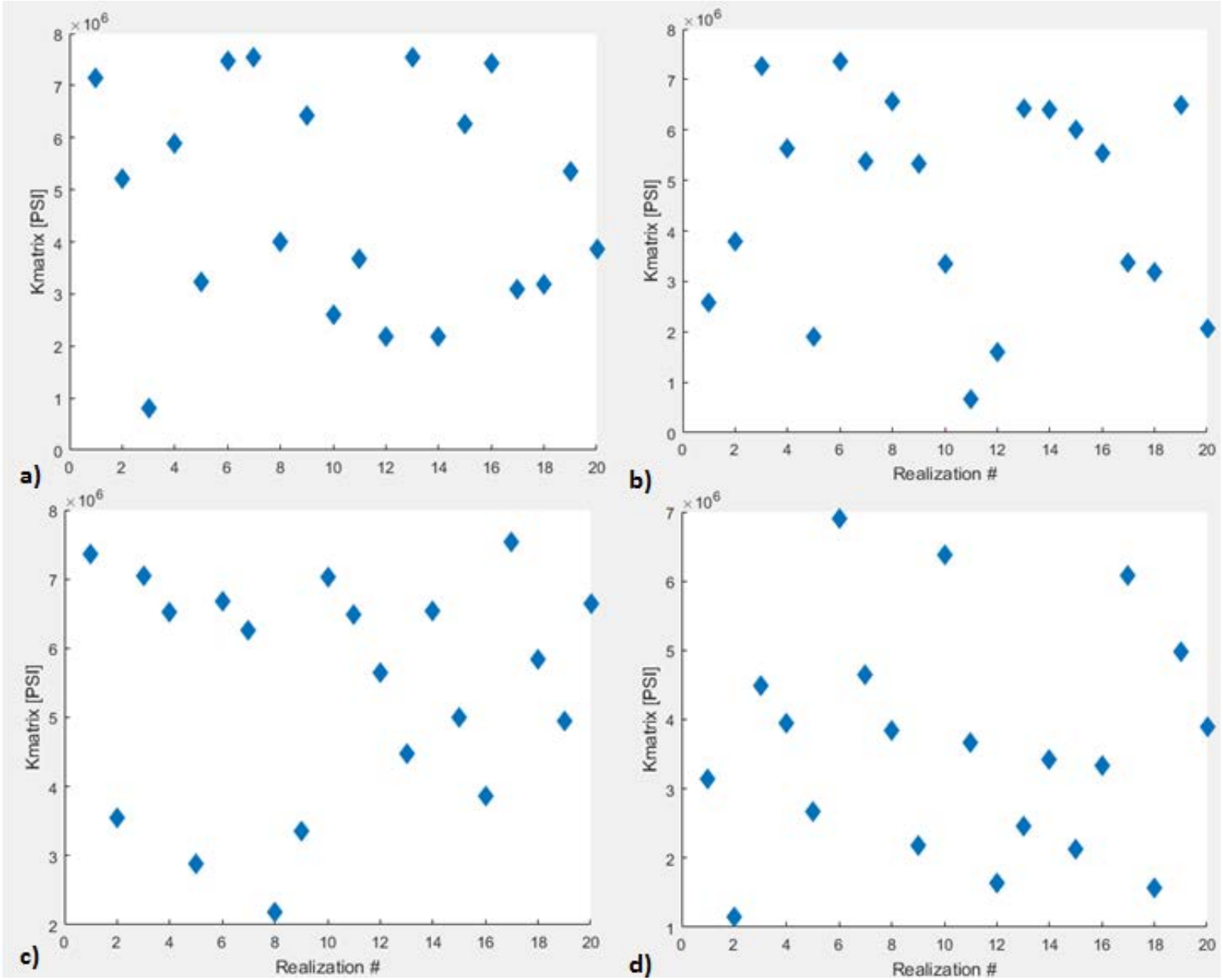

Figure 6. Dry rock bulk modulus computed for 20 realizations at selected 3D gridblock indices: (a) (17, 1, 1) (rock type = 2); (b) (12, 35, 85) (rock type = 1); (c) (32, 21, 32) (rock type = 3), and (d) (17, 5, 109) (rock type = 4).

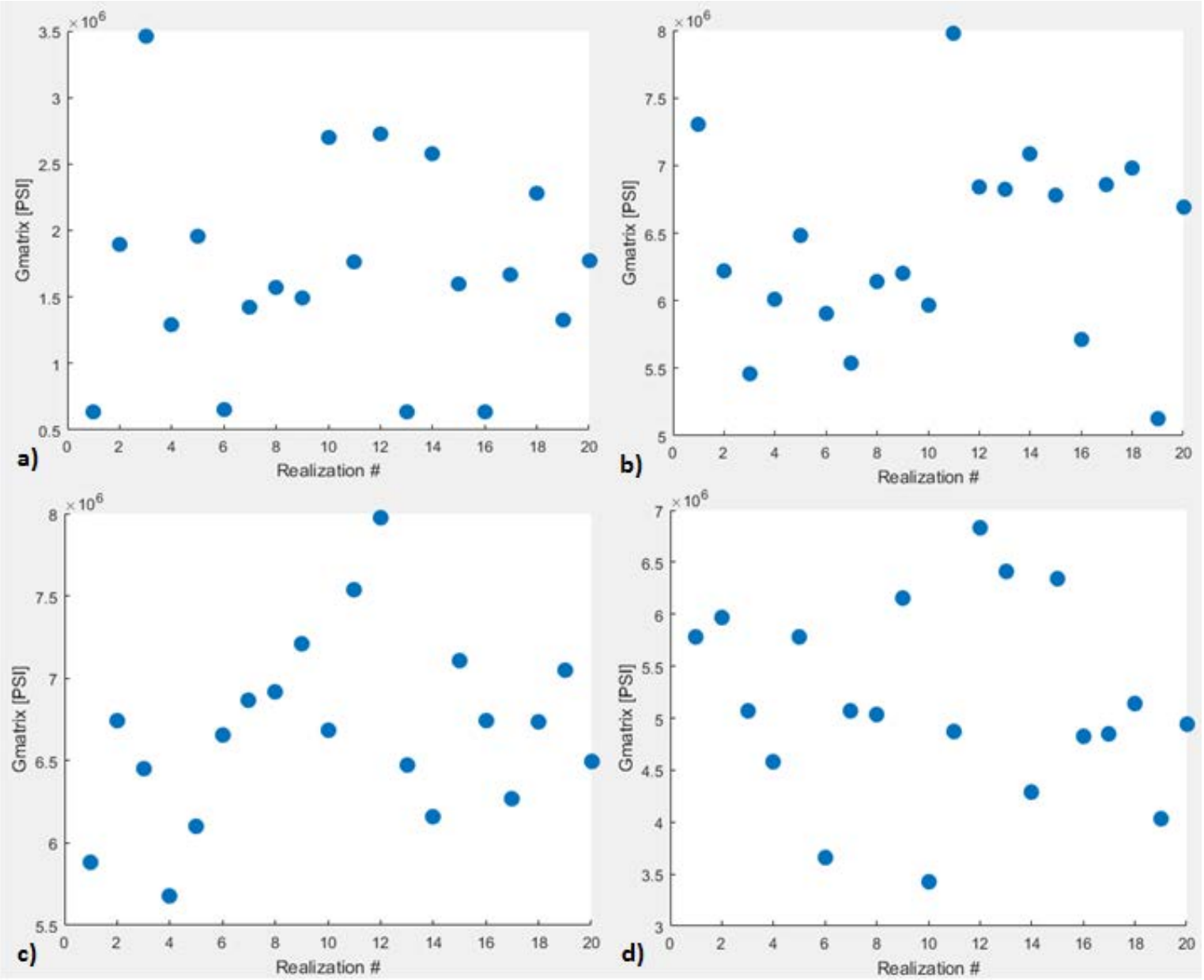

Figure 7. Shear Bulk Modulus computed for 20 realizations at selected 3D gridblock indices: (a) (17, 1, 1) (rock type = 2); (b) (12, 35, 85) (rock type = 1); (c) (31, 21, 32) (rock type = 3), and (d) (17, 5, 109) (rock type = 4).

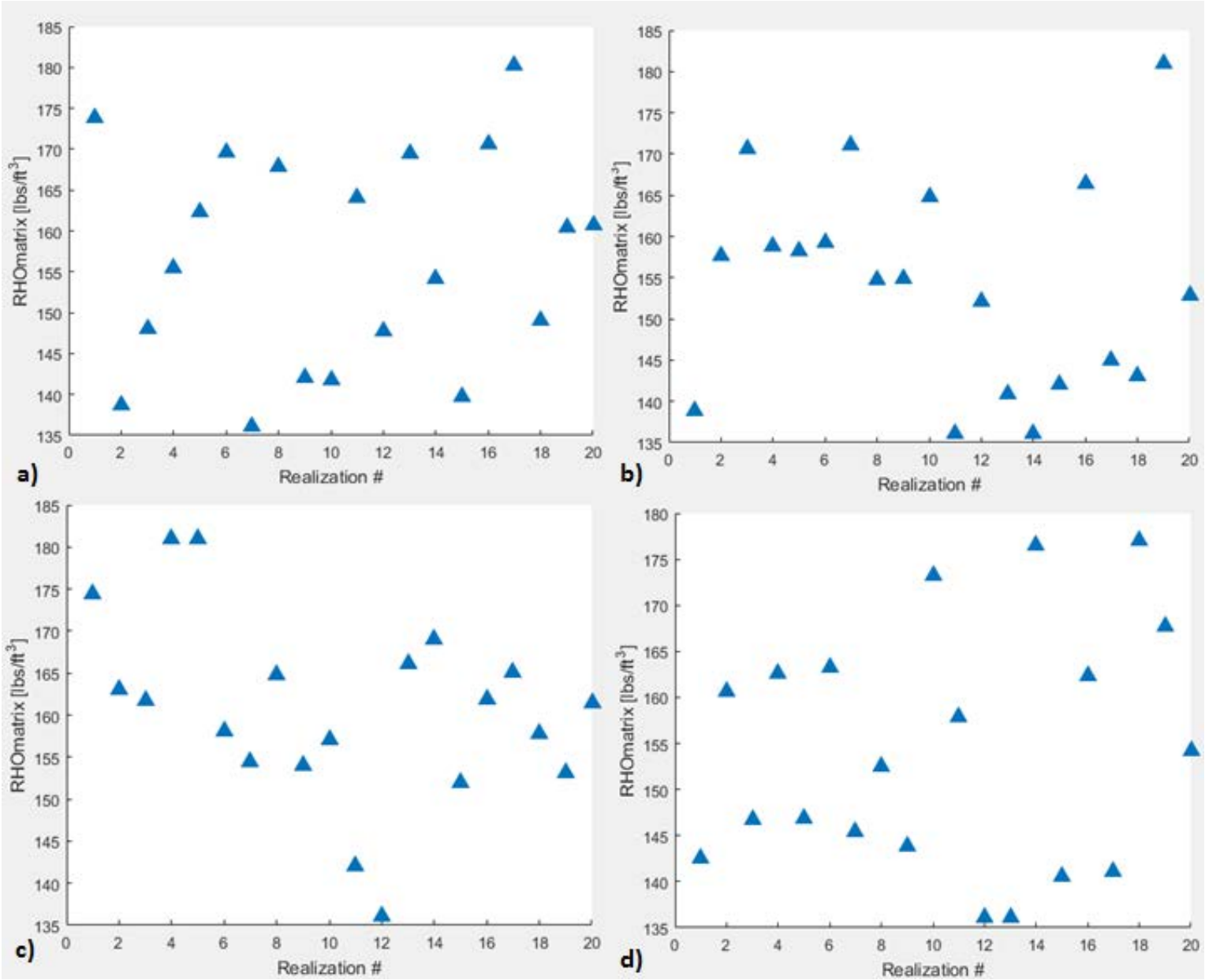

Figure 8. Dry rock matrix density computed for 20 realizations at selected 3D gridblock indices: (a) (17, 1, 1) (rock type = 2); (b) (12, 35, 85) (rock type = 1); (c) (32, 21, 32) (rock type = 3), and (d) (17, 5, 109) (rock type = 4).

a)

Property	Mean	Std. (+/-)
K_{matrix}	4.7521e+06	2.1310e+06
G_{matrix}	1.7037e+06	7.7113e+05
Rho_{matrix}	156.6087	13.1828

b)

Property	Mean	Std. (+/-)
K_{matrix}	4.5486e+06	2.0750e+06
G_{matrix}	6.4059e+06	7.0206e+05
Rho_{matrix}	154.2492	12.6697

c)

Property	Mean	Std. (+/-)
K_{matrix}	5.4919e+06	1.6114e+06
G_{matrix}	6.6872e+06	5.4650e+05
Rho_{matrix}	160.7227	11.1471

d)

Property	Mean	Std. (+/-)
K_{matrix}	3.6262e+06	1.6161e+06
G_{matrix}	5.1531e+06	9.2119e+05
Rho_{matrix}	154.3709	13.1485

Table 1. Summary statistics for K_{matrix} in psi, G_{dry} (G_{matrix}) in psi, and ρ_{matrix} (Rho_{matrix}) in lbm/ft^3 for Gridblocks: (a) (17, 1, 1) (rock type = 2); (b) (12, 35, 85) (rock type = 1); (c) (32, 21, 32) (rock type = 3); and (d) (17, 5, 109) (rock type = 4).